MDPI

Article

SNOWTRAN: A Fast Radiative Transfer Model for Polar Hyperspectral Remote Sensing Applications

Alexander Kokhanovsky [1,*] , Maximilian Brell [1], Karl Segl [1] and Sabine Chabrillat [1,2]

1   Helmholtz Center Potsdam GFZ German Research Centre for Geosciences, 14473 Potsdam, Germany;
    maximilian.brell@gfz-potsdam.de (M.B.); karl.segl@gfz-potsdam.de (K.S.);
    sabine.chabrillat@gfz-potsdam.de (S.C.)
2   Institute of Soil Science, Leibniz University Hannover, 30419 Hannover, Germany
*   Correspondence: kokhanov@gfz-potsdam.de

Abstract: In this work, we develop a software suite for studies of *atmosphere–underlying SNOW-spaceborne optical receiver* light TRANsmission calculations (SNOWTRAN) with applications for the solution of forward and inverse radiative transfer problems in polar regions. Assuming that the aerosol load is extremely low, the proposed theory does not require the numerical procedures for the solution of the radiative transfer equation and is based on analytical equations for the spectral nadir reflectance and simple approximations for the local optical properties of atmosphere and snow. The developed model is validated using EnMAP and PRISMA spaceborne imaging spectroscopy data close to the Concordia research station in Antarctica. A new, fast technique for the determination of the snow grain size and assessment of the snowpack vertical inhomogeneity is then proposed and further demonstrated on EnMAP imagery over the Aviator Glacier and in the vicinity of the Concordia research station in Antarctica. The results revealed a large increase in precipitable water vapor at the Concordia research station in February 2023 that was linked to a warming event and a four times larger grain size at Aviator Glacier compared with Dome C.

Keywords: EnMAP; PRISMA; hyperspectral measurements; top-of-atmosphere reflectance; snow albedo; snow grain size; snow optics

1. Introduction

Radiative transfer modeling is an important tool for simulating and studying the interaction of radiation with different underlying surfaces and the atmosphere in order to make better use of remote sensing data. Multiple radiative transfer codes exist for the simulation of satellite signals at the top of atmosphere (TOA) (see, e.g., [1–8]). Papers [2–8] are aimed at the solution of the general radiative transfer in various turbid media. In contrast, ref. [1] has a special target: the spectral TOA reflectance over snow. The authors of [1] rely on the numerical solution of the radiative transfer equation (RTE), which slows down the calculation procedure considerably.

A new generation of spaceborne imaging spectroscopy sensors has been appearing in recent years (e.g., EnMAP, PRISMA [9,10]), and they have the capacities to observe polar areas on demand with high spatial and spectral resolution, covering the broad spectral range of 400–2500 nm. Furthermore, the next generation is preparing for operational, regularly repeating satellite measurements, including polar areas such as CHIME [11] and SBG [12], which will significantly increase the amount of observation data. In this frame, the task of this paper is to develop a fast and accurate radiative transfer code for the simulation of hyperspectral satellite measurements over Antarctica and other polar regions with underlying snow surfaces based on the approximate analytical solutions of the RTE, which will be applicable to current and future nadir-looking imaging spectroscopy missions. The Sobolev approximation [13] is used to simulate the radiative transfer in the atmosphere. This approximation is valid at small values of the average cosine of scattering

angle g, which is a valid approximation, e.g., over Antarctica, where the aerosol load is extremely low; therefore, the light scattering is mostly due to molecules. It is known that $g = 0$ for molecular scattering. The spherical albedo of semi-infinite homogeneous snow surfaces is considered in the framework of the van de Hulst approximation valid at any level of light absorption in snow [14,15]. We have extended the van Hulst approximation to the case of the nadir reflectance as observed by hyperspectral instruments orbiting our planet at present (see, e.g., [9,10]). Furthermore, we have used the analytical representation of both the aerosol phase function and aerosol spectral extinction coefficient, which makes it possible to avoid time-consuming Mie calculations or the usage of respective look-up-tables. We have found that the shortwave infrared (SWIR) TOA reflectance spectra closely coincide with the spectra of the underlying surface modulated by the atmospheric gaseous absorption processes in this case. This is due to the weak aerosol load in polar regions.

The first version of a software suite for studies of *atmosphere–underlying SNOW-spaceborne optical receiver* light TRANsmission calculations (SNOWTRAN) has been proposed in [16] for the spectral range of 400–1000 nm. In this paper, we extend the range of the applicability of SNOWTRAN to the spectral region of 320–2500 nm using the extended databases of absorption cross-sections of atmospheric molecules such as O_2, O_3, and H_2O. The local (single-scattering albedo, asymmetry parameter) and global (reflectance, albedo) snow optical properties are also calculated at any level of light absorption, making it possible to extend the range of the applicability of the respective equations and software to the shortwave infrared (SWIR) region. The main advantage of SNOWTRAN is the possibility to perform fast and accurate radiative transfer calculations for an atmosphere–underlying snow system in both clean and polluted snow cases.

2. The Analytical Representation of the Top-of-Atmosphere Reflectance over Snow

2.1. The Radiative Transfer in a Snow Layer

The top-of-atmosphere (TOA) reflectance over snow R_{TOA}, as used in version 1.1 of the SNOWTRAN software, is given by the following analytical expression [16]:

$$R_{TOA} = RT_g, \tag{1}$$

where T_g is the gaseous transmittance; R is the TOA reflectance of the gaseous absorption free atmosphere–underlying snow surface, derived as

$$R = R_a + \gamma T_a R_s , \tag{2}$$

R_a is atmospheric reflectance for the case of a black underlying surface, T_a is the two-way atmospheric transmittance, and R_s is the snow reflectance (bottom-of-atmosphere (BOA) reflectance). The parameter γ accounts for the atmosphere–snow retro-reflections. The value of γ can be calculated using the following approximation that is strictly valid for the Lambertian underlying surfaces [16]:

$$\gamma = (1 - r_a r_s)^{-1}, \tag{3}$$

where r_a is the atmospheric albedo and r_s is the snow spherical albedo.

It is assumed that the snow can be represented as a semi-infinite layer with irregularly shaped ice crystals. The spherical albedo of such a layer with the single-scattering albedo ω_0 and the asymmetry parameter g can be estimated using the following approximation [14]:

$$r_s = \frac{(1 - as)(1 - s)}{(1 + bs)}, \tag{4}$$

where $a = 0.139$, $b = 1.17$, and

$$s = \sqrt{\frac{(1 - \omega_0)}{(1 - g\omega_0)}} \tag{5}$$

is the similarity parameter. It follows from Equation (4) that various turbid media with close values for the similarity parameter *s* have similar spherical albedo values. The approximation given by Equation (4) is very accurate and can be used at any level of light absorption in snow, which is relevant for the modeling of visible-near-infrared (VNIR) and SWIR snow spectra.

In this paper, we derive the relevant approximation for the value of the nadir snow reflectance R_s, which is accurate in both the VNIR and SWIR regions. In principle, R_s can be found solving the respective integro-differential radiative transfer equation [13,15]. It is assumed in the framework of SNOWTRAN that the nadir snow reflectance can be calculated using the following approximation derived from the parameterization of the simultaneous radiative transfer calculations of the snow reflectance R_s and spherical albedo r_s, as presented in [15]:

$$R_s = a_0 + a_1 r_s + a_2 r_s^2, \qquad (6)$$

where the parameters a_0, a_1, a_2 depend on the cosine of the solar zenith angle μ_0 (see Appendix A). The accuracy of Equations (4) and (6) is demonstrated in Figure 1 for the case of the Henyey–Greenstein phase function [13,15] with the asymmetry parameters *g* equal to 0.75 and 0.875 (typical for snow [17]) and several values of the single-scattering albedo ω_0.
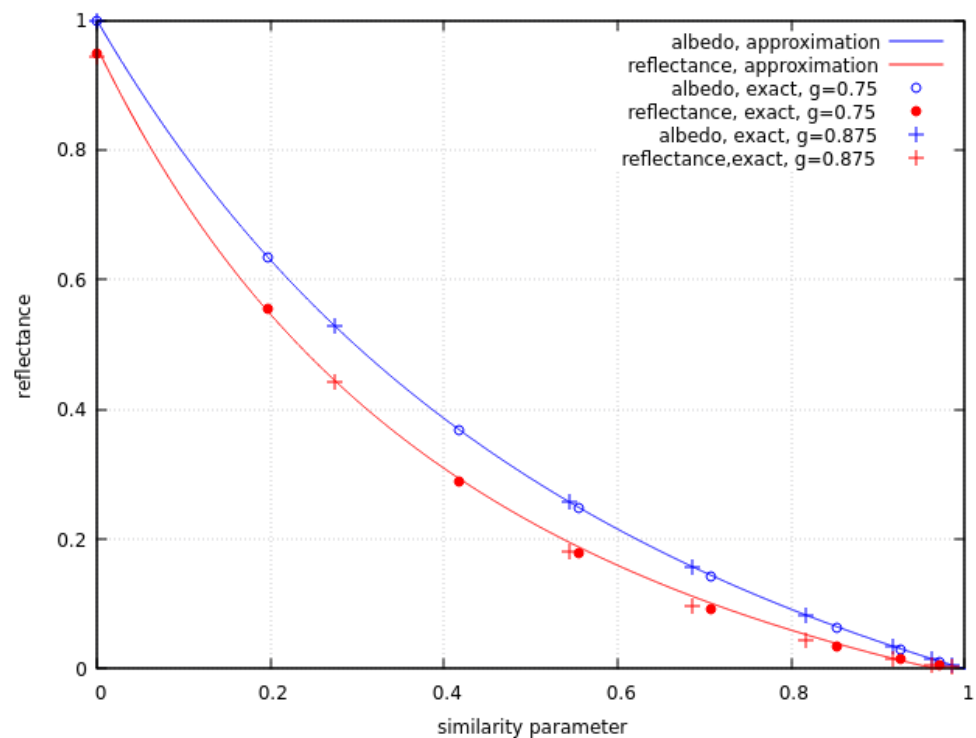
Figure 1. The accuracy of the approximation for the spherical albedo (blue line) and nadir reflectance (red line) at the solar zenith angle of 60 degrees.

Equations (4), (5), and (6) make it possible to calculate the global radiative transfer characteristics of snow layers for a given value of the similarity parameter *s*. It follows from Equation (5) that the similarity parameter *s* depends on just two local optical characteristics of snow (ω_0 and *g*). Therefore, an important point is to find analytical relationships of these parameters with the size of ice grains. This also makes it possible to reduce the number of input parameters for the model proposed in this paper. Under the assumption of clean snow, we shall use the following approximate equations for the relevant parameters [17,18]:

$$\omega_0 = 1 - \beta_i, \ \beta_i = \frac{1}{2}(1 - \rho)(1 - e^{-\sigma z}), g = g_\infty - (g_\infty - g_0)e^{-\varepsilon z} \qquad (7)$$

derived using the geometrical optics approximation for the fractal ice grains [17,19]. Here, β_i is the probability of photon absorption (PPA) by pure snow at the wavelength λ, $\alpha = 4\pi\chi/\lambda$, $z = \alpha d_{ef}$ is the bulk ice absorption coefficient, χ is the imaginary part of the ice refractive index, and d_{ef} is the effective diameter of ice grains; parameters $\rho, \sigma, \varepsilon, g_0, g_\infty$ depend on the assumed type/shape of ice crystals in snow. The effective grain diameter is defined as [17,20,21]:

$$d_{ef} = \frac{3V}{2\Sigma}. \tag{8}$$

where V is the average volume of the ice grains and Σ is their average cross-section perpendicular to the incident beam. It is assumed that particles are randomly oriented.

We have found that the volume of fractal grains used in simulations (Koch fractals of the second generation [19]) is related to the side length ℓ by the following formula:

$$V = b\ell^3, \tag{9}$$

where $b = 27/52\sqrt{2} \approx 0.367$. Then, it follows that $d_{ef} = \varsigma\ell^3/\Sigma$, where $\varsigma = 1.5b$. The numerical calculations show that the value of d_{ef} is close to $\ell/2$.

We use the following equations for the parameters ρ, g_0, g_∞, derived for the real part of the refractive index n in the range of 1.25–1.35, which is the case for ice in the spectral region of 0.3–2.5 µm [17,22]:

$$\rho = 0.0123 + 0.1622(n-1), \ g_0 = 0.9919 - 0.769(n-1),$$
$$g_\infty = 1.008 - 0.11(n-1). \tag{10}$$

In addition, when fitting the numerical Monte Carlo geometrical optical calculations with the use of Equation (7), we found that $\sigma = 0.9045$ and $\varepsilon = 0.8571$. These parameters depend on the assumed shapes of ice crystals in snow.

The extinction cross-section of large, nonspherical, randomly oriented particles can be calculated as follows [20,21]:

$$C_{ext} = 2\Sigma. \tag{11}$$

Therefore, it follows for the extinction coefficient [17] that:

$$k_{ext} = \frac{3c}{d_{ef}}, \tag{12}$$

where c is the volumetric concentration of particles. Taking into account that c is close to $1/3$ for natural snow covers [17], it is concluded that the extinction length in snow $L_{ext} = k_{ext}^{-1}$ is close to the effective diameter of ice grains.

The intercomparison of results derived using the simple equations in (7) and time-consuming geometrical optical Monte Carlo calculations [18] is shown in Figure 2a,b for the case of large nonspherical particles (Koch fractals of the second generation [18] with the side length of the initial tetrahedron ℓ equal to 50, 100, and 300 µm (or $d_{ef} = 0.027, 0.054,$ and 0.162 mm, respectively). The ice spectral refractive index proposed in [22] has been used. The high accuracy of the methods in Equation (7) is clearly demonstrated. Some deviations could be actually due to the statistical error of Monte Carlo calculations and not due to the errors of Equation (7). Figure 2c shows the results of the calculation of the similarity parameter s using Equations (5) and (7), and the Monte Carlo geometrical optics calculations. Both results almost coincide, which makes it possible to derive the analytical relationship between the value of the nadir reflectance (see Equations (4) and (6)) and the effective diameter of ice grains, which is of importance for the solution of the inverse snow optics problems.
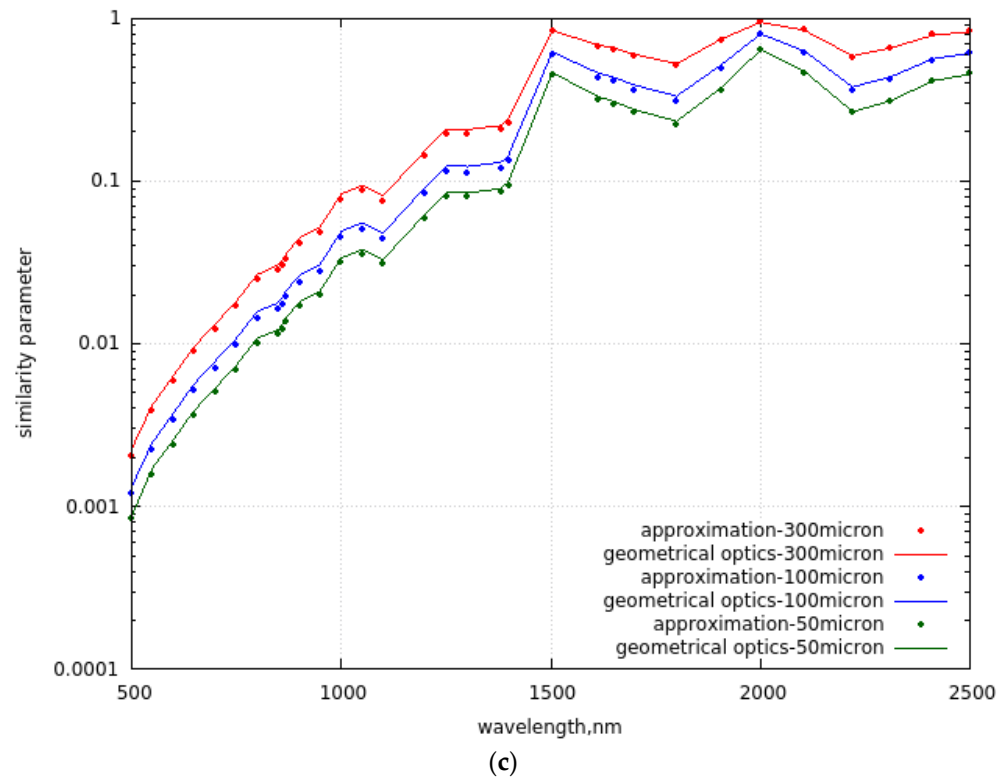
(**a**)

(**b**)

Figure 2. *Cont.*

(c)
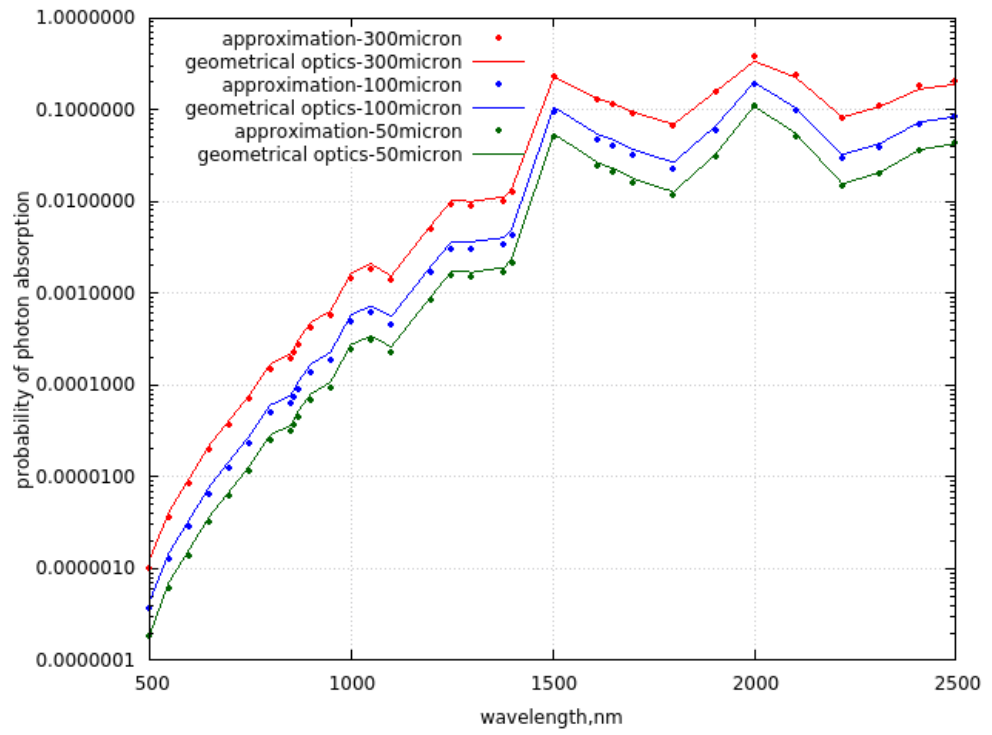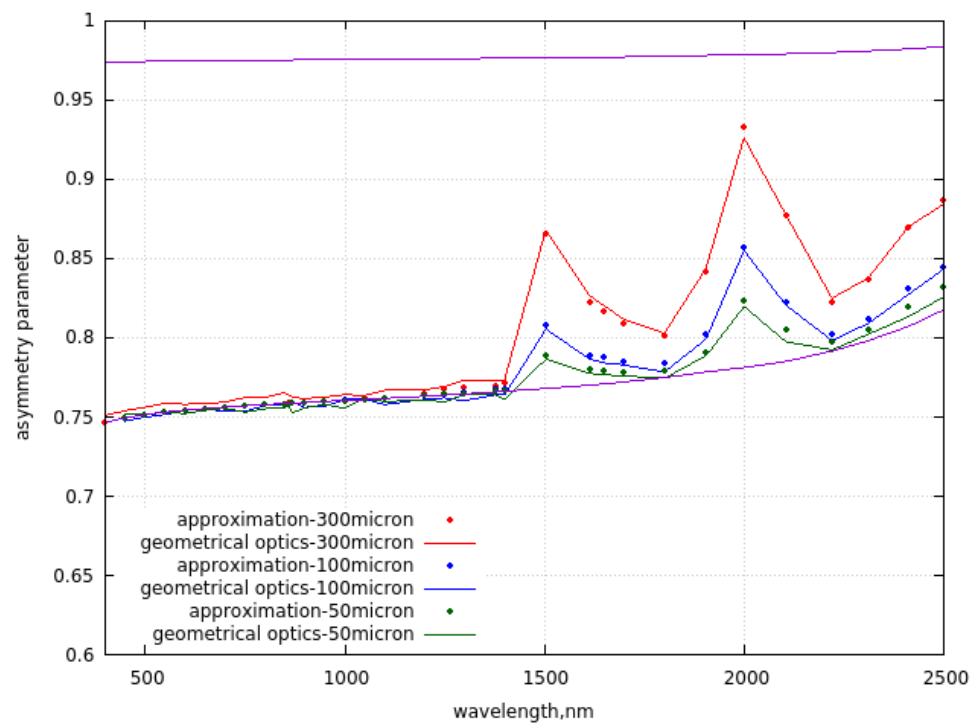
Figure 2. (**a**). The spectral dependence of the probability of photon absorption, derived using the geometrical optics Monte Carlo code (lines) and simple Equation (7) (symbols) for the length ℓ of the side of the initial ice tetrahedron for the Koch fractal of the second generation [17] equal to 50, 100, and 300 μm. (**b**) The same as in (**a**) except the asymmetry parameter is considered. The lower and upper lines give the spectral dependencies of the parameters g_0 (lower line) and g_∞ (upper line) (**c**). The same as in (**a**) except for the similarity parameter.

We have studied the case of type 1 snow (clean snow) in the discussion given above. Let us consider now the case of type 2 snow (snow with impurities). The level of snow pollution is usually low; therefore, in a good approximation, we can assume that the light scattering and extinction processes in snow are dominated by ice grains. The absorption coefficient of snow with impurities can be presented as:

$$k_{abs} = c_i \kappa_i + c_p \kappa_p, \tag{13}$$

where c_i is the volumetric concentration of ice grains and c_p is the volumetric concentration of impurities. We assume that just one type of impurity is present in the snow, although the technique can easily take into account multiple types of impurities by adding additional terms in Equation (13). The values of κ_i and κ_p are the volumetric absorption coefficients of ice grains and impurities, respectively. They can be calculated as follows:

$$\kappa_i = \frac{\langle C_{abs,i} \rangle}{\langle V_i \rangle}, \ \kappa_p = \frac{\langle C_{abs,p} \rangle}{\langle V_p \rangle}, \tag{14}$$

where $\langle C_{abs,i} \rangle$ is the average absorption cross-section of ice grains, $\langle V_i \rangle$ is the average volume of ice grains, $\langle C_{abs,p} \rangle$ is the average absorption cross-section of impurities, and $\langle V_p \rangle$ is the average volume of impurities. It follows for the probability of photon absorption that:

$$\beta \equiv \frac{k_{abs}}{k_{ext}} = \beta_i + c_p \frac{\kappa_p}{k_{ext}}, \tag{15}$$

where β_i is the PPA for snow without impurities (see Equation (7)); thus (see Equations (12) and (15)):

$$\beta = \beta_i + \frac{cd_{ef}}{3}\kappa_p, \tag{16}$$

where $c = c_p/c_i$. One can see that the probability of photon absorption for the snow with impurities not only depends on the value of β_i but also on the relative volumetric concentration of impurities c and their spectral volumetric absorption coefficient κ_p. We shall parameterize the spectrum κ_p in the following way:

$$\kappa_p(\lambda) = \kappa_p(\lambda_0)(\lambda/\lambda_0)^{-m}, \tag{17}$$

where $\kappa_0 = \kappa_p(\lambda_0)$ and m are the input parameters of the discussed analytical model. We shall assume that $\lambda_0 = 550$ nm.

2.2. The Atmospheric Radiative Transfer

Let us consider the atmospheric radiative transfer processes now. It is assumed that the polar atmosphere is clean and is the main contribution to light scattering and extinction in atmosphere is due to molecular scattering. Therefore, we use the same approach for the calculation of the atmospheric characteristics (r_a, R_a, T_a) as that described in [16]. The input for the atmospheric model is the spectral aerosol optical thickness τ_{aer}, presented as $\tau_{aer} = (\lambda/\lambda_0)^{-B}\tau_{aer}(\lambda_0)$, where $\tau_{aer}(\lambda_0)$ is the aerosol optical thickness at the wavelength $\lambda_0 = 550$ nm [16] and B is the Angström parameter. The molecular optical thickness is calculated as suggested in [16]. The gaseous transmittance T_g in Equation (1) is found using the following approximation [16]:

$$T_g = T_{H_2O}T_{O_2}T_{O_3}, \tag{18}$$

where gaseous transmittances for water vapor, oxygen, and ozone are given by the following expressions:

$$T_{H_2O} = \exp(-(Mf_{H_2O}\tau_{H_2O})^\varsigma), \; T_{O_2} = \exp(-(Mf_{O_2}\tau_{O_2})^\upsilon), \; T_{O_3} = \exp(-M\tau_{O_3}). \tag{19}$$

Here, M is the airmass factor, $f_{H_2O} = (P/P_0)^{m_{H_2O}}(T_0/T)^{p_{H_2O}}$, $f_{O_2} = (P/P_0)^{m_{O_2}}(T_0/T)^{p_{O_2}}$. The pair (T_0, P_0) represents normal temperature (273.16 K) and pressure (1013.25 hPa), and the values (T, P) give the average values of temperature and pressure over vertical for a given location. The parameters ς, υ, $m_{H_2O}, p_{H_2O}, m_{O2}, p_{O_2}$ depend on the absorption band. The optical thicknesses for various gaseous absorbers are calculated as follows:

$$\tau_{H_2O} = k_{abs,H_2O}\ell_{H_2O}, \; \tau_{O_2} = k_{abs,O_2}\ell_{O_2}, \; \tau_{O_3} = C_{abs,O_3}N_{O_3} \tag{20}$$

where k_{abs,H_2O} is the absorption coefficient of water vapor (cm^{-1}), ℓ_{H_2O} is the precipitable water vapor (PWV) measured in cm, k_{abs,O_2} is the molecular oxygen absorption coefficient (cm^{-1}), ℓ_{O_2} is the total molecular oxygen column (TMOC) (cm), N_{O_3} is the total ozone column (in Dobson Units (DU)), and C_{abs,O_3} is the absorption cross-section of ozone molecule in the inverse DU (the multiplier 2.69×10^{16} should be applied to transfer C_{abs,O_3} (usually provided in the units $cm^2/molec$) to the inverse Dobson Units).

The vertical profile of molecular oxygen concentration could be considered as a constant one compared with the highly variable profiles of ozone and water vapor concentrations. Let us introduce the effective oxygen vertical column: $L_{O_2} = f_{O_2}\ell_{O_2}$. Then, it follows that $T_{O_2} = \exp(-(ML_{O_2}k_{abs,O_2})^\upsilon)$. Therefore, for the calculation of the oxygen transmittance, we use the value of L_{O_2}, which reduces the number of parameters needed for the calculations. More precisely, the normalized effective oxygen amount (NOX) K_{O_2} is used as an input in SNOWTRAN. It is defined as follows: $K_{O_2} = L_{O_2}/\ell^{st}_{O_2}$, where $\ell^{st}_{O_2} = 87068.53$ cm

is the molecular oxygen vertical column of the standard atmosphere [8]. The value of K_{O_2} is equal to the ratio $\ell_{O_2}/\ell_{O_2}^{st}$ at $f_{O_2} = 1$.

We use the parameters ς, υ, m_{H_2O}, p_{H_2O} and spectra $k_{abs,H_2O}(\lambda)$, k_{abs,O_2}, C_{abs,O_3}, provided in [8] at the spectral resolution of 7 nm (the triangular slit function has been used) in steps of 1 nm. In addition, we have calculated the oxygen absorption coefficient using the approximation provided in [23] for the oxygen absorption band located at the wavelength 1.27 μm, which is not provided in [8].

The geometrical approximation for the airmass factor has been used:

$$M = \xi^{-1} + \eta^{-1}. \tag{21}$$

Here, ξ, η are the cosines of the solar and observation zenith angles, respectively.

The example of calculations using SNOWTRAN for the case of polluted snow is given in Figure 3. The values of the parameters used in the calculations are given in Table 1.
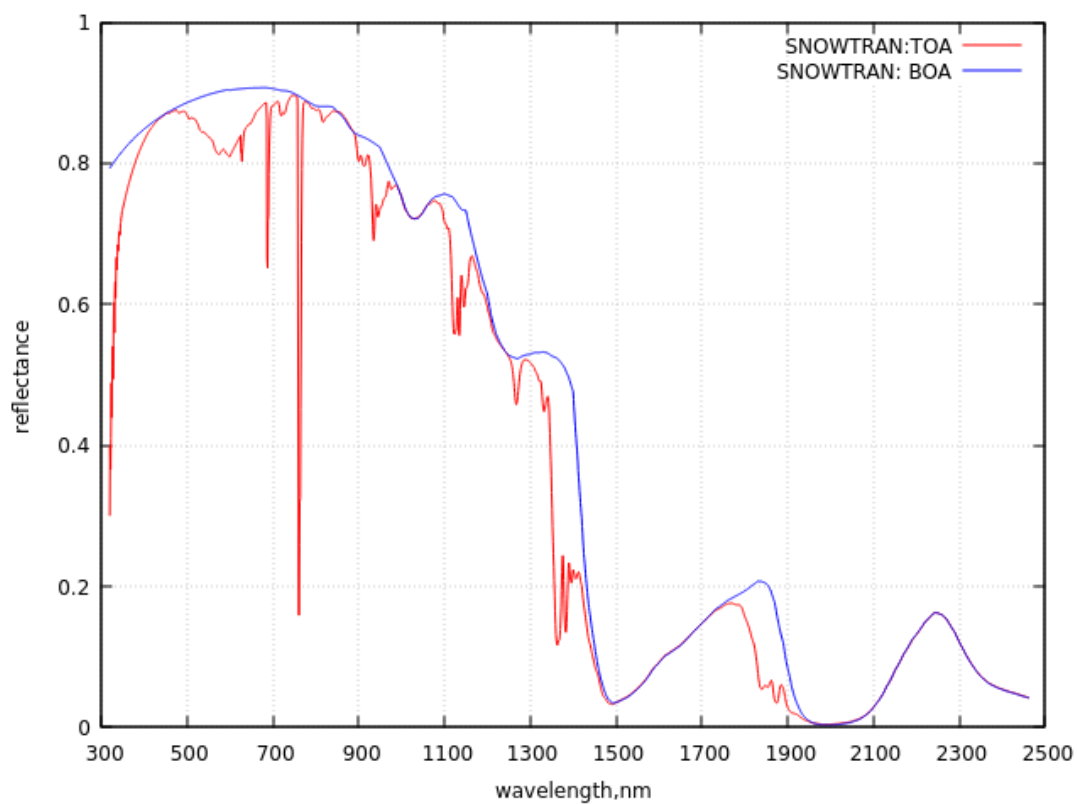
Figure 3. The spectral dependence of the BOA and TOA spectral reflectance of atmosphere—underlying dust—polluted snow system simulated using SNOWTRAN at the nadir observation and solar zenith angle equal to 60 degrees.

Table 1. The parameters used in the simulations shown in Figure 3.

Parameter	Physical Meaning	Value
d_{ef}, mm	Effective grain diameter	0.2
TOC, DU	Total ozone column (TOC)	289
PWV, cm	Precipitable water vapor (PWV)	0.055
K_{O_2}	Normalized effective oxygen column (NOX)	0.9
$\tau_{aer}(550\text{ nm})$	Aerosol optical thickness (AOT) at 550 nm	0.02
B	Aerosol Angström parameter	1.8

Table 1. *Cont.*

Parameter	Physical Meaning	Value
c, ppm	Relative impurity concentration	50.0
$\kappa_p(550\ \text{nm})$, $1/\mu\text{m}$	Volumetric impurity absorption coefficient	0.04
m	Impurity absorption Angström parameter	4.0
H, m	Surface height	3233
P_s, hPa	Surface pressure	651
T, K	Average temperature along vertical	229
P, hPa	Average pressure along vertical	491

## 3. The Comparison of Theoretical Calculations with Satellite Measurements

Let us compare SNOWTRAN calculations with spaceborne hyperspectral measurements over Antarctica. We will use data of the German spaceborne imaging spectrometer mission EnMAP [10,24] and the Italian Space Agency imaging spectrometer mission PRISMA [9].

EnMAP performs the spectral radiance measurements at a spatial resolution of 30 m in the spectral range of 418–2450 nm, with an average spectral sampling distance of 6.5 nm in VNIR and 10 nm in SWIR (https://www.enmap.org/, accessed on 1 January 2024). The measurements are performed using two separate spectrometers (VNIR and SWIR). PRISMA (https://www.eoportal.org/satellite-missions/prisma-hyperspectral, accessed on 1 January 2024) has the same spatial resolution, and a spectral range of 407–2469 nm is covered with a spectral sampling interval of $\leq$ 12 nm in both VNIR and SWIR (https://www.prisma.asi/, accessed on 1 January 2024). The conversion of the spectral radiance I provided in the L1C EnMAP data and PRISMA top-of-atmosphere radiance data to the spectral reflectance R has been performed using the following equation:

$$R = \frac{\pi I}{\xi d_{sol} F_{sol}}, \tag{22}$$

where the parameter d_{sol} accounts for the Sun–Earth distance and F_{sol} is the solar irradiance at the top-of-atmosphere, which was also considered for the radiometric calibration of the sensor. The latter is important because TOA reflectance should be independent of the solar model, which is not the case if two different models are used. Therefore, we have applied the solar irradiance model given in [25] in the case of EnMAP and the model provided in [26] in the case of PRISMA.

Figures 4 and 5 show SNOWTRAN results compared with EnMAP and PRISMA at different spectral resolutions, respectively, and Table 2 resumes the simulation parameters for both cases. The spectral reflectance derived from the EnMAP measurements for a single pixel located at (75.119°S, 123.902°E) is given in Figure 4a together with the calculations of the top-of atmosphere and bottom-of-atmosphere (BOA) snow reflectance. The EnMAP measurements have been performed on 15 February 2023 at 00:36 UTC. We have used the values of a surface pressure of 651 hPa, surface height of 3233 m, and average values of pressure and temperature along vertical equal to 491 hPA and 229 K, as in our previous publication [27]. The values of TOC (250DU) and PWV (0.175 cm) were taken coincidentally with those measured at the closely located Concordia research station (Dome C, 75S, 123.3°E). Other parameters used in the SNOWTRAN simulations are given in Table 2. They have been selected by fitting SNOWTRAN and satellite measurements at several spectral points. It follows from Figure 4a that SNOWTRAN is indeed capable of efficiently describing the EnMAP hyperspectral satellite measurements.
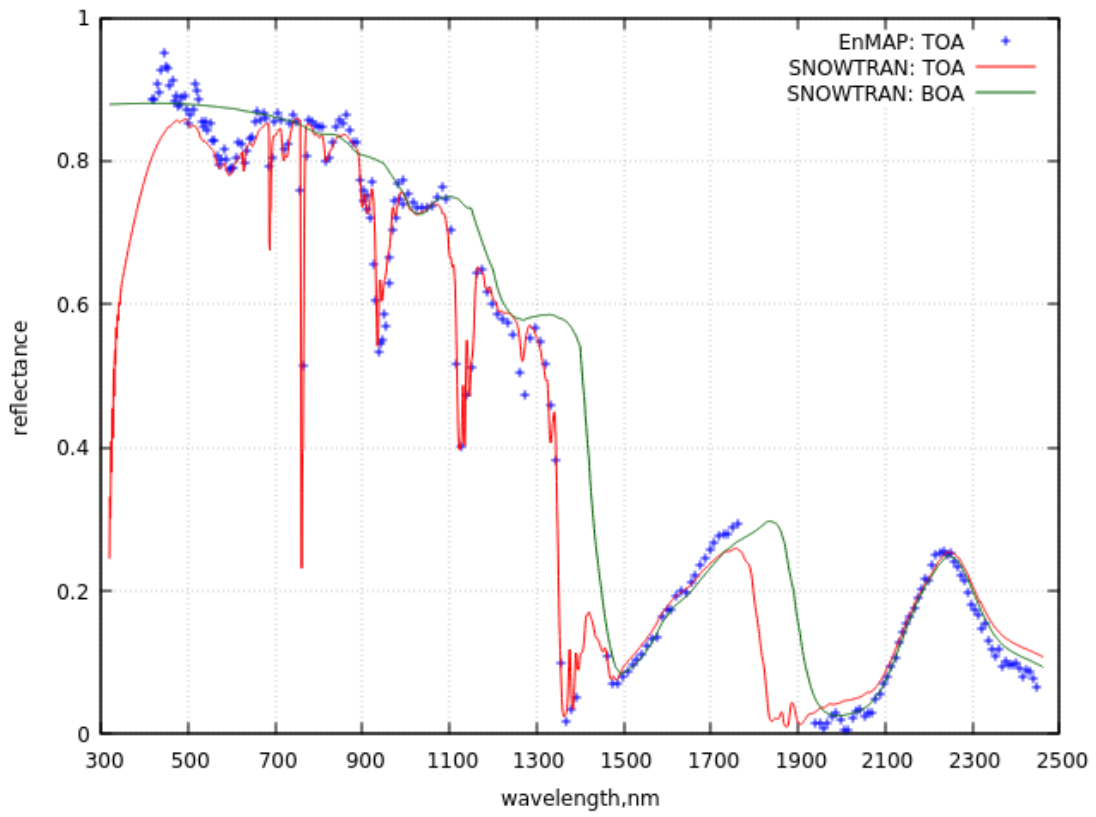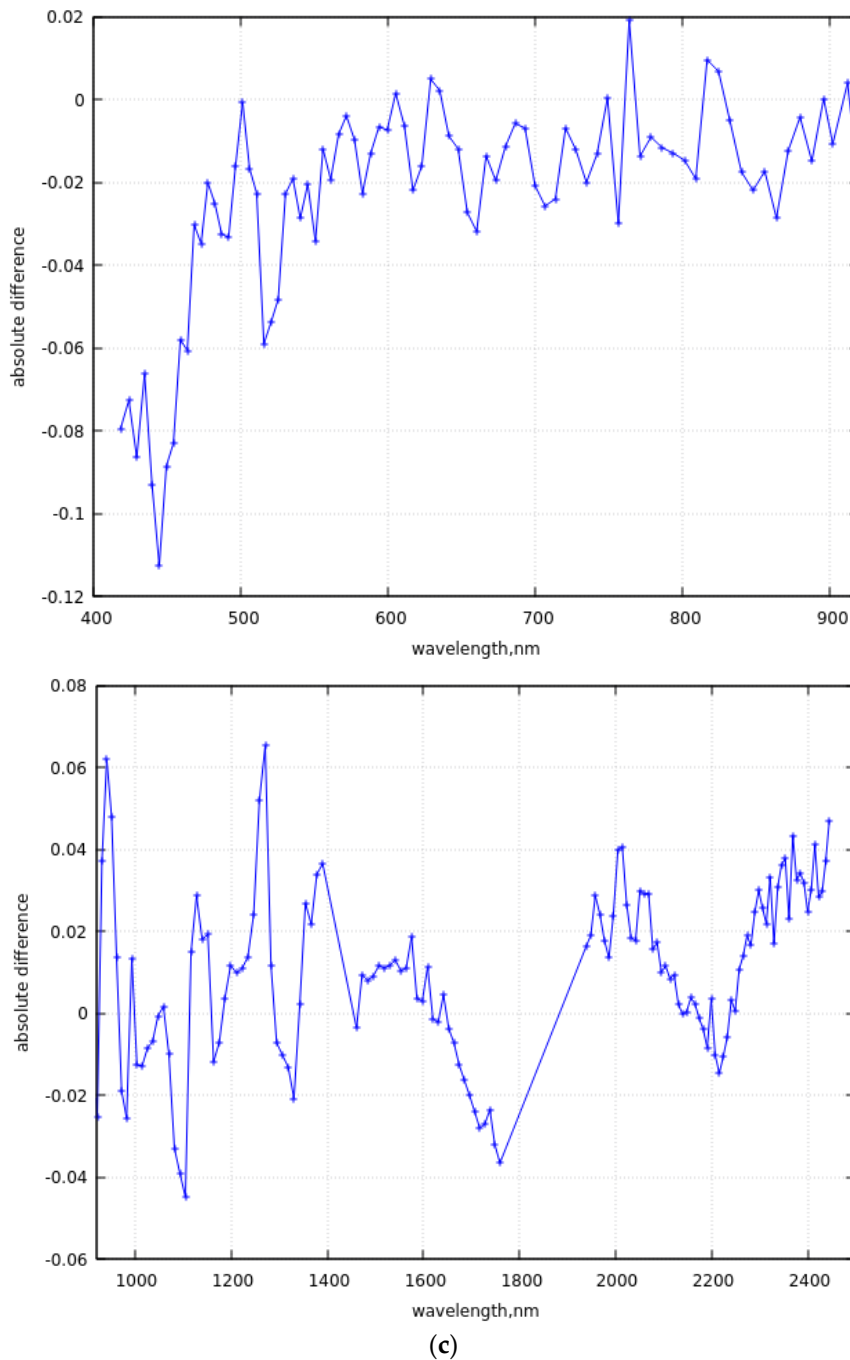
(**a**)
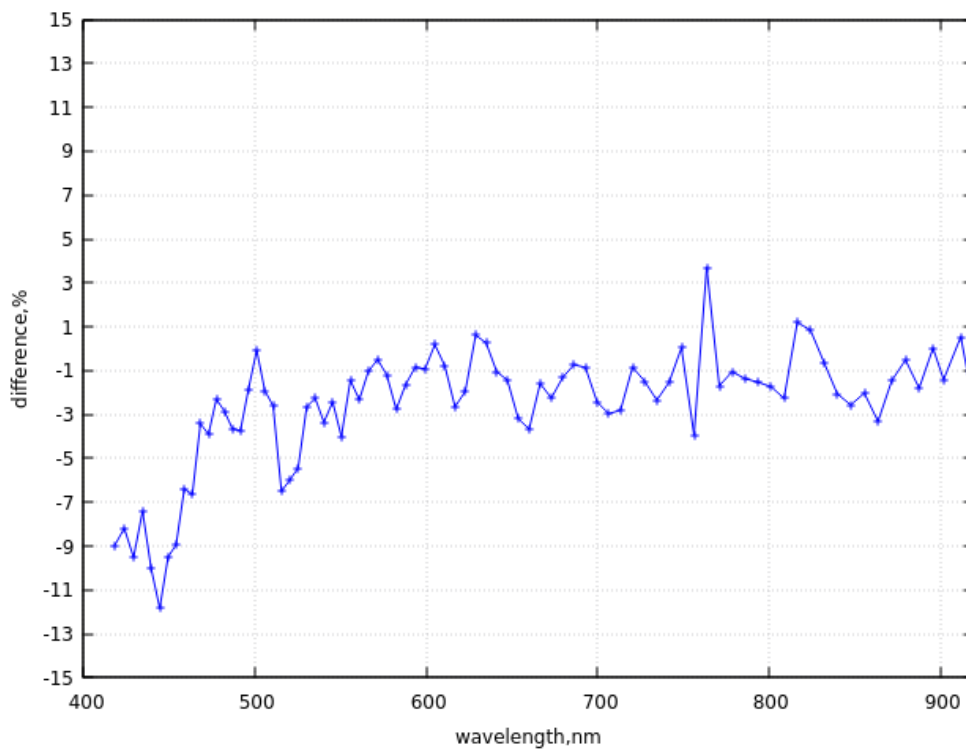
(**b**)

Figure 4. *Cont.*

Figure 4. (**a**) The intercomparison of SNOWTRAN spectra with the EnMAP measured spectra (75.119S,123.902E, 15 February 2023, 00:36 UTC). The EnMAP data in the spectral range with strong water vapor absorption (e.g., around 1800 nm) are not provided by the satellite ground system. (**b**) The relative difference (in percent) between theoretical calculations and experimental data in the VNIR region. (**c**) The absolute difference between theoretical calculations and experimental data in VNIR (upper panel) and SWIR (lower panel).

The reason for the deviations of the theoretical calculations and EnMAP measurements in the range of 418–500 nm for bright snow surfaces must be further investigated. It is unlikely that they are related to the inaccuracy of the SNOWTRAN model. Some deviations of theoretical calculations in gaseous absorption bands are due to the different spectral sampling of SNOWTRAN (1 nm) and EnMAP (6.4–10 nm) measurements.

We have resampled the SNOWTRAN data derived with 1 nm spectral resolution to match the spectral sampling and spectral instrument response function of EnMAP. The difference between the resampled SNOWTRAN data and EnMAP spectra in the spectral range of 418–920 nm and 920–2500 nm is given in Figure 4b,c. One can see that the difference is smaller than 2% for most of points not contaminated by gaseous absorption, which is an excellent result both with respect to the SNOWTRAN and EnMAP performance. The differences are somewhat larger in SWIR (see Figure 4c), which is explained by the influence of gaseous absorption bands, especially water vapor. The difference in gaseous absorption bands needs a more thorough analysis, possibly accounting for other gaseous absorbers and the change in the assumed abundance of atmospheric gaseous components in the SNOWTRAN run. The errors related to the integration of the oscillating spectral radiance in the gaseous absorption bands with respect to the EnMAP spectral response function could also be of importance.

The fit of PRISMA measurements at the location (76.14S, 129.93E) situated at a somewhat larger distance from the ground validation site located at Dome C is given in Figure 5a. The measurements have been taken on 21 December 2022 at 00:14:07 UTC. We also see that the SNOWTRAN model can be successfully used to simulate the TOA PRISMA spectral reflectance. The ground observations at DOME C give TOC = 269 DU and PWV = 0.045 cm at the same date and time. These parameters are somewhat smaller than the parameters used in the simulations (289 DU and 0.055 cm, respectively). The parameters used in the simulations have been selected to provide the best fit of experimental and theoretical curves in the ozone and water vapor absorption bands. Therefore, they can be considered as retrieved characteristics. The possible explanation for the differences between ground and satellite-derived parameters could be due to an inexact collocation of ground and satellite measurements and also due to corresponding experimental errors of the related retrieval techniques. The spectral relative and absolute difference of PRISMA data and resampled SNOWTRAN calculations are given in Figure 5b,c. The resampling has been performed to match the spectral sampling and spectra instrument response function for PRISMA. One can see that the relative difference is not larger than 5% in the deep blue region in contrast to the difference with EnMAP data shown in Figure 4b.
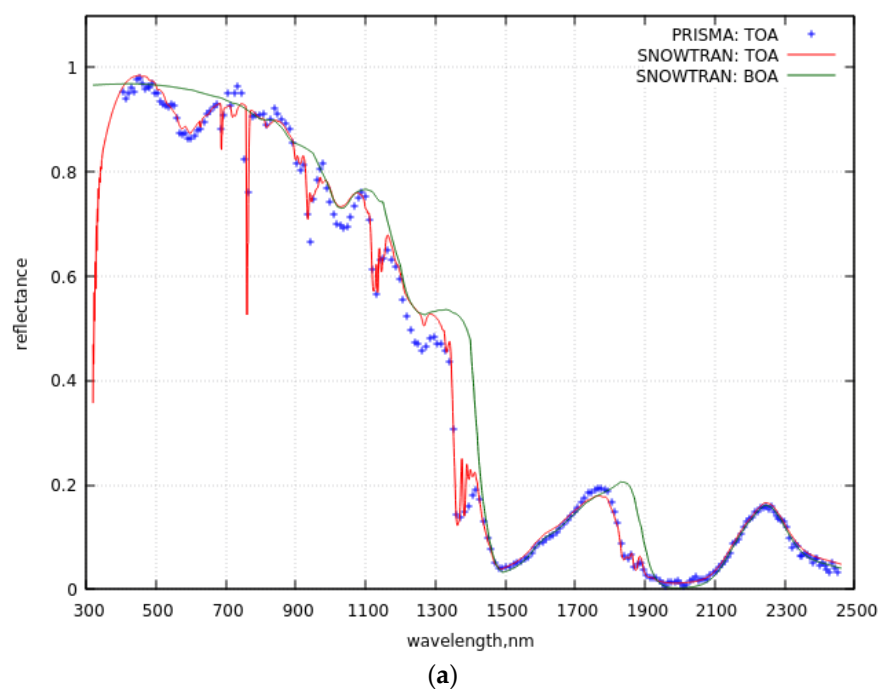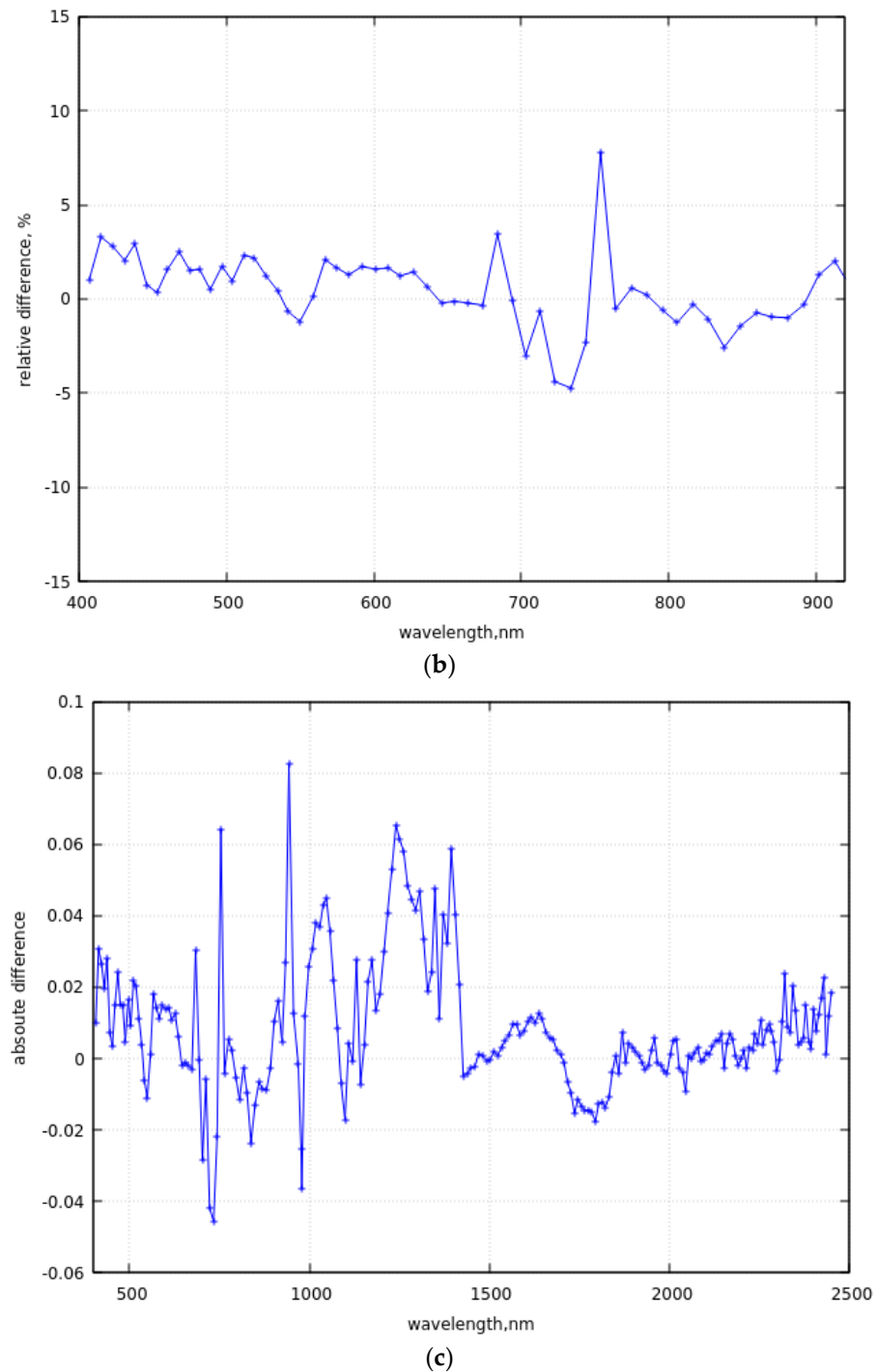

(a)

Figure 5. *Cont.*

(**b**)

(**c**)

Figure 5. (**a**) The intercomparison of SNOWTRAN spectra with the PRISMA measured spectra (76.14°S,129.93°E, 21 December 2022, 00:14UTC). (**b**) The spectral relative difference (in percent) between the theoretical calculations and PRISMA data in the VNIR region. (**c**) The spectral absolute difference between the theoretical calculations and PRISMA data.

Table 2. The parameters of the model used in simulations for the case of the nadir observations shown in Figures 4a and 5a. The ground-observed TOC and PWV at Dome C (75S, 123.3E) are given in brackets. It has been assumed that the snow is free of impurities. The small difference in satellite measurements (up to 5 degrees) from the exact nadir direction is ignored.

Parameter	EnMAP 15 February 2023	PRISMA 21 December 2022
d_{ef}, mm	0.11	0.2
TOC, DU	250	289 (269)
PWV, cm	0.175	0.055 (0.045)
TOX	0.45	0.13
τ_{aer} (550 nm)	0.14	0.05
B	1.0	1.35
ϑ_o, degrees	68.0	57.6
Latitude, degrees	75.119°S	76.140°S
Longitude, degrees	123.902°E	129.930°E
Date/time (UTC)	15 February 2023/ 00:36 UTC	21 December 2022/ 00:14 UTC

It follows from Figure 4a that EnMAP measurements can be well fitted using SNOW-TRAN both at 1030 nm and 2200 nm bands, which are almost free of gaseous absorption and atmospheric scattering effects. This is not the case for the PRISMA measurements (see Figure 5a). This points to the fact that at the time and location of PRISMA measurements, the snow vertical inhomogeneity cannot be ignored. This brings us to the conclusion that snow vertical inhomogeneity could be potentially assessed using hyperspectral top-of-atmosphere reflectance measurements [28,29]. Also, we can see that SNOWTRAN calculations and PRISMA measurements at 1500–2500 nm (and also for EnMAP, see Figure 4a) matches very well. This points out that this spectral range can be used to derive the snow grain size in the upper snow layer due to the small penetration depth of the SWIR radiation in snow. This subject is considered in the next section.

One concludes from Figures 4a and 5a that the TOA reflectance is smaller than the BOA reflectance in the gaseous absorption bands. In some channels, the BOA reflectances are slightly smaller than the TOA reflectances. This is related to the uncertainties of the SNOWTRAN model. However, it should be underlined that the respective errors are smaller compared with the calibration errors of the hyperspectral measurements.

Currently, investigations are ongoing for the differences in the spectral range of 418–464 nm (see Figure 4a) between the SNOWTRAN and EnMAP data. Such differences and small-scale oscillations as seen in Figure 4b have been found for water surfaces as well. They might be related to the calibration of EnMAP data, which is indirectly supported by the data shown in Figure 5a for PRISMA, where respective differences in the deep blue region of the electromagnetic spectrum are much smaller.

4. The Determination of the Snow Grain Size

In this section, we consider the application of the proposed theoretical framework (forward model) for the determination of the snow grain size from EnMAP measurements. It is an important fact that both albedo and nadir reflectance primarily depend on just one parameter characterizing the snow microstructure (the similarity parameter *s*). Therefore, the inverse problem is reduced to the determination of the snow microstructure from the

value of the similarity parameter s. This parameter can be directly retrieved from the measurements of r_s or R_s, i.e., it follows from Equation (4) that:

$$s = \frac{\psi - \sqrt{\psi^2 - 4a(1 - r_s)}}{2a},$$

(23)

where $\psi = 1 + a + br_s$. One can see that $s = 0$ at $r_s = 1$ and $s = 1$ at $r_s = 0$, as it should be (see Figure 1 and Equation (4)). The value of r_s can be measured directly or derived from the nadir reflectance (see Equation (6)):

$$r_s = \frac{\sqrt{a_1^2 - 4a_2(a_0 - R_s)} - a_1}{2a_2}.$$

(24)

Equations (5) and (7) can be used to determine the value of the effective grain size from the value of the similarity parameter s analytically. Namely, it follows that:

$$d_{ef} = \frac{1}{\alpha\sigma} \ln\left[\frac{\phi/s^2 + \gamma_1}{\phi/s^2 - \gamma_2}\right],$$

(25)

where α is the bulk ice absorption coefficient at the wavelength λ, $\phi = \frac{1}{2}(1 - \rho)$, $\gamma_1 = g_\infty - g_0$, $\gamma_2 = 1 - g_\infty$. The derivation of Equation (25) has been performed at the assumption $\varepsilon = \sigma$ (see Equation (7)), which is a valid approximation for the case under study.

One can see that the value of d_{ef} can be derived analytically from the values of r_s or R_s (see Equations (23)–(25)). It is of importance that the values of s, r_s, and R_s depend on the wavelength and d_{ef} does not (for vertically homogeneous snow layers). Therefore, the spectral dependence of d_{ef} is an indication of the snow vertical inhomogeneity. We select the measured reflectance at the wavelengths of 1030 nm, 1235 nm, and 2200 nm, which are least affected by the atmospheric scattering and absorption processes (see Figure 4a) and are also sensitive to the snow grain size. Then, it follows that $R_{TOA} \approx R_s$ (see Equations (1) and (2) and Figure 3).

Due to the different penetration of radiation in vertically inhomogeneous snow at different wavelengths [17], the values of d_{ef} derived at different wavelengths may differ. Let us introduce the ratio of effective diameters retrieved at 1235nm ($d_{ef,1235\text{nm}}$) and 2200 nm ($d_{ef,2200\text{nm}}$) to that at 1030 nm ($d_{ef,1030\text{nm}}$):

$$K_1 = \frac{d_{ef,2200\text{nm}}}{d_{ef,1030\text{nm}}}, \quad K_2 = \frac{d_{ef,1235}}{d_{ef,1030\text{nm}}}.$$

(26)

It should be noted that it can generally be assumed that $K_1 < K_2$ because the SWIR radiation with longer wavelengths generally penetrates to the smaller distances from the snow top, where new fresh fallen snow with smaller crystals are located. The radiation with a wavelength of 1235 nm can penetrate into somewhat deeper snow layers as compared with that at a wavelength of 2200 nm.

We have derived the values of $d_{ef,1030\text{nm}}$, $d_{ef,1235\text{nm}}$, and $d_{ef,2200\text{nm}}$ for the EnMAP 30 km × 30 km scene located at the Aviator Glacier in Antarctica (16.02.2023 at 22:11 UTC). A glacier is a mass of ice with sufficient thickness to flow away from the source area in lobes, tongues, or masses. The results are given in Figure 6a–c.

(**a**)

(**b**)

(**c**)
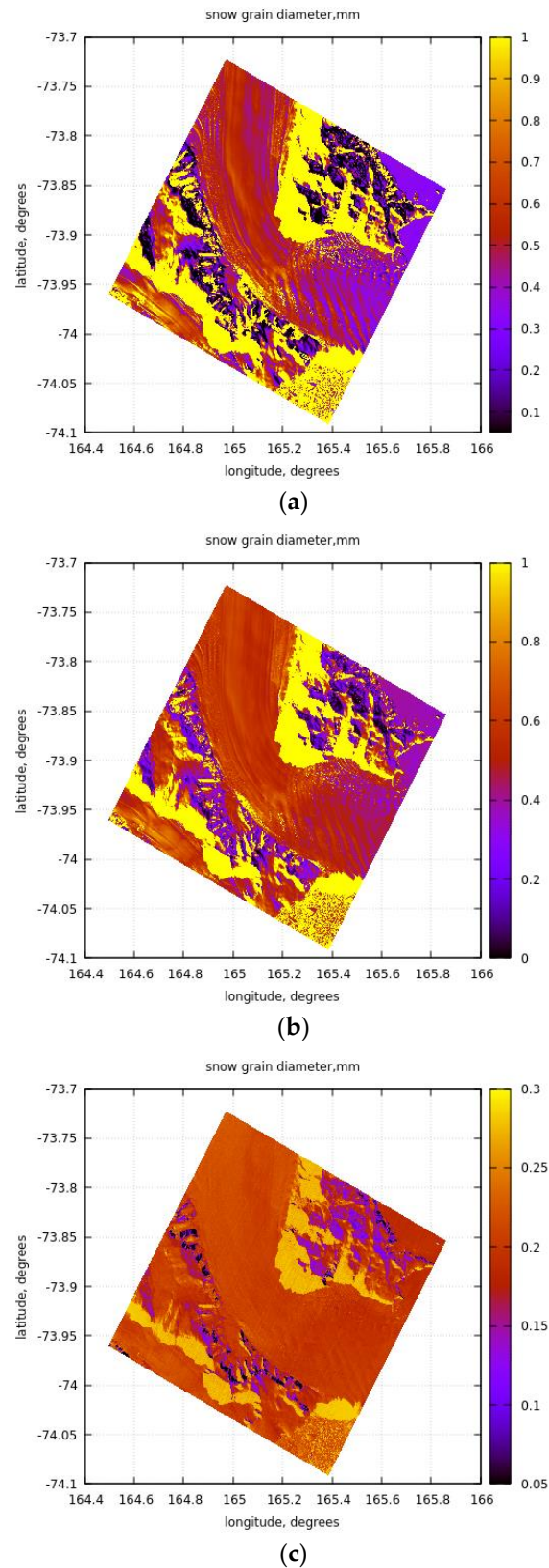
Figure 6. The retrieved spatial distribution of snow grain diameter (mm) based on the values $d_{ef,1030nm}$ (**a**), $d_{ef,1235nm}$ (**b**), and $d_{ef,2200nm}$ (**c**) over the Aviator glacier based on EnMAP reflectance measurements.

The valid results are given in the central part of the picture (Aviator Glacier Tongue) between two mountainous areas, where the ice flow to the ocean occurs. One can see that the value of $d_{ef,1235\text{nm}} \approx d_{ef,1030\text{nm}}$ and $d_{ef,2200\text{nm}} < d_{ef,1030\text{nm}}$ is as one may expect. In particular, we have found that $d_{ef,1030\text{nm}} \approx 0.52$ mm, $d_{ef,1235\text{nm}} \approx 0.58$ mm, $d_{ef,2200\text{nm}} \approx 0.21$ mm, $K_1 = 0.4$, and $K_2 = 1.1$ for the area **A** (73.75S–73.85S, 165–165.1E). Hence, the sizes of ice crystals at the top ($d_{ef,2200\text{nm}}$) are more than two times smaller compared with the sizes inside the snow layer ($d_{ef,1030\text{nm}}$), as one might expect due to the snow metamorphism processes. The spatial distribution of the parameter K_1 is given in Figure 7. It should be pointed out that although the parameter d_{ef} is affected by the assumed shape of light scattering particles [17], this is less the case for the ratios K_1 and K_2 due to the cancellation of a common multiplier.
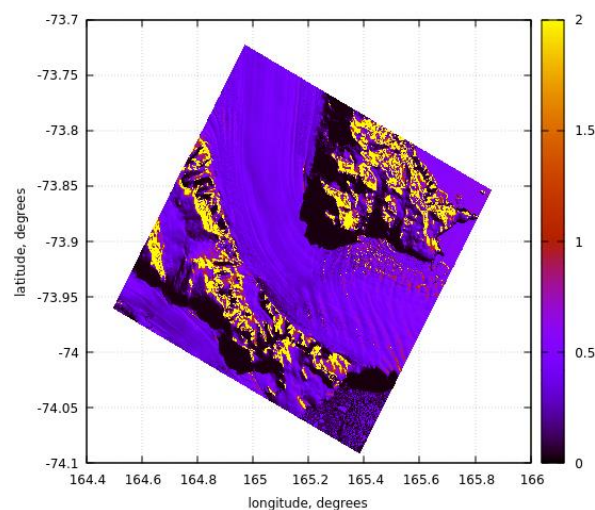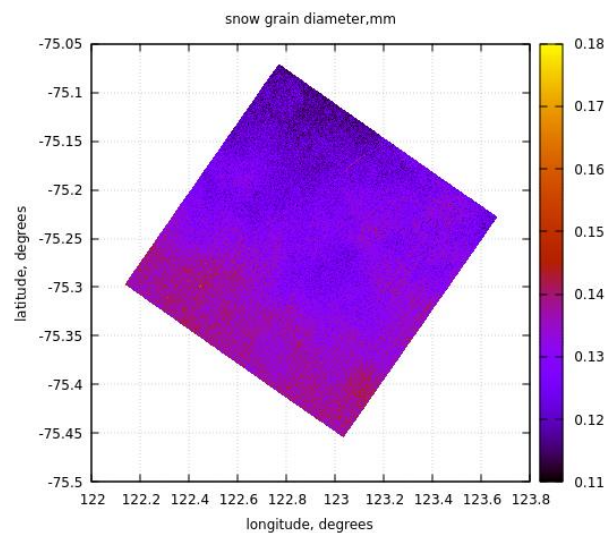

Figure 7. The spatial distribution of the parameter K_1 over the Aviator Glacier.

The retrievals for the case of vertically inhomogeneous snow requires the change of the forward model, which is out of the scope of this paper. Because the value of K_1 is close to one, one may expect that the snow observed using the couple of wavelengths of 1030 and 1235 nm can be considered as a homogeneous one. Therefore, the algorithm proposed in [27] is valid for the case considered here. Indeed, we have derived the value of $d_{ef,0} = d_{ef,1} = 0.53$ mm from the algorithm described in [27] for the area **A** (see above), which is close to the value of $d_{ef,1030\text{nm}}$ derived in the framework of the algorithm discussed in this paper. It should be pointed out that the presented algorithm and the one described in [27] are based on a different system of equations. Therefore, our conclusions confirm the consistency of both algorithms, even though the current algorithm is able to determine the grain sizes at the very top of the snow surface, which is not the case for the algorithm described in [27]. Although we do not have grain sizes measured in situ and collocated with satellite measurements, our results are consistent with those presented in [30], where the most frequent grain size diameters are in the range of 0.2–0.4 mm at another coastal Antarctic site (67.7S, 139.72E, Adelie Land). More validation work is needed to relate the satellite-measured snow grain size with in situ-derived values of the same parameter.

The snow grain size derived from EnMAP measurements at another location (closer to DOME C) using a 1030 nm band is shown in Figure 8. It is obvious that the spatial distribution of the retrieved snow grain size is not as pronounced as in the case of the Aviator Glacier due to the reduced number of factors influencing the snow metamorphism processes (e.g., precipitation, surface inclination, proximity to the ocean, and mountains). The average grain diameter derived from the 1030 nm EnMAP measurements is 0.13 mm, which is close to the range of diameters (0.15–0.3 mm) measured at the site close to Dome C [30]. The spatial distribution of the ice grain diameter derived from the EnMAP measurements at 2200 nm is somewhat smaller (0.1 mm), with the spatial distribution being similar

to that shown in Figure 8. Basically, we can conclude that the vertical inhomogeneity of the snow is less pronounced compared with the Aviator Glacier case shown in Figure 6, where the sizes at the top and inside the snow differ by more than two times, being larger at larger depths inside the snow. The small vertical variability of snow grain size around Dome C has been found using ground measurements as well [30].

Figure 8. The snow grain size spatial distribution in the vicinity of DOME C (75°S, 123.3°E, 26 October 2022, 00:33 UTC), Concordia research station.

It should be pointed out that the application of 2200 nm channel to the snow grain size retrieval must be performed only for the case of small ice crystals. With the increase in the crystal size, the reflectance at this channel saturates, and the information on the snow grain size is lost (see Figure 9). The same applies to the 1640 nm channel.
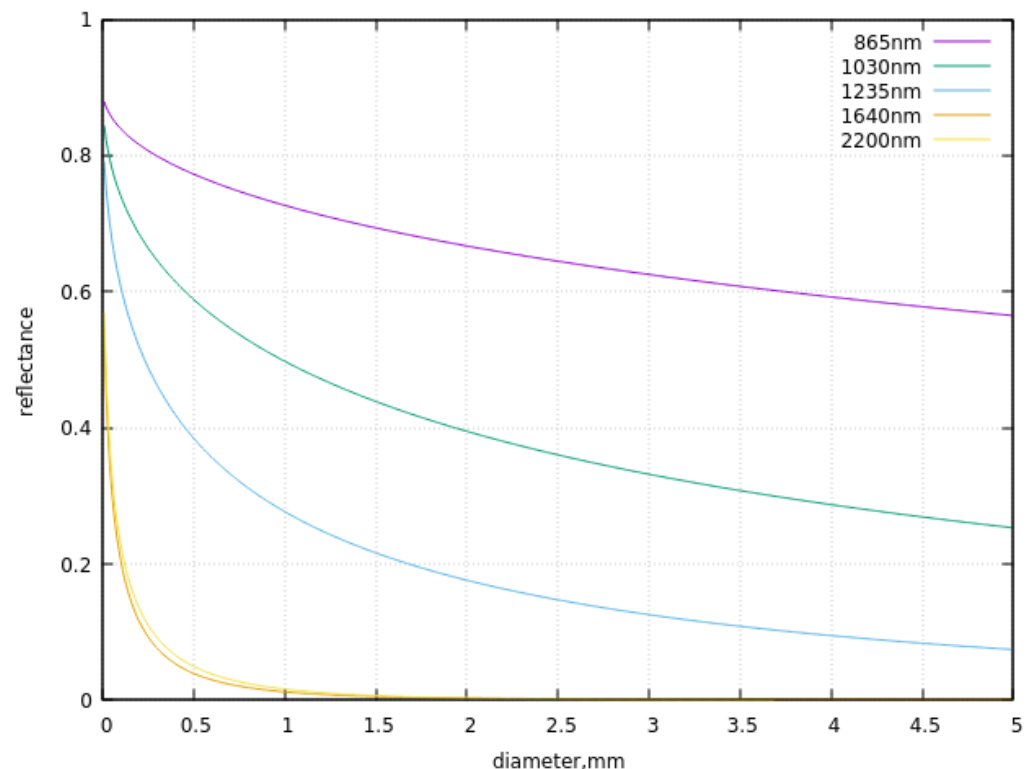
Figure 9. The dependence of the nadir snow reflectance on the diameter of grains in snow at the solar zenith angle equal to 60 degrees.

The EnMAP data can not only be used for the determination of snow parameters but also for the characterization of atmospheric state over the snow field, as discussed in [27]. In particular, we have found a significant difference in the value of the precipitable water vapor at Dome C on 15 February 2023 as compared with 21 December 2022 (see Table 2). This peculiarity is explained by the advective warming event at Dome C on 15 February 2023 reported in [31].

5. Conclusions

We have proposed a fast and simple fully analytical model for the calculation of the TOA reflectance over snow surfaces. The derived equations have also been used to derive the snow grain size, which can be used to estimate other snow parameters such as snow spectral and broadband albedo, bottom-of-atmosphere reflectance and snow specific surface area. It has been assumed that the snow is an ideally horizontal semi-infinite homogeneous surface without sastrugi and any inclination. The model can be easily extended to consider Mie scattering by atmospheric particles and to account for inclined surfaces. The case of nadir observations common for current and future hyperspectral missions was considered. The technique can be easily extended to the case of off-nadir observations, if needed. The simplicity of the model makes it possible to apply the developed software for the solution of the inverse problem, i.e., the determination of atmosphere and underlying snow properties from hyperspectral satellite observations, as demonstrated here for EnMAP measurements. In particular, we have found a significant difference in the value of the precipitable water vapor (PWV) at Dome C on 15 February 2023 as compared with 21 December 2022 (see Table 2).

Although the derived expression for the nadir snow reflectance as a function of the effective grain size is only an approximation to the exact radiative transfer solution for the case of clean Antarctic atmosphere [32], the radiative transfer in natural snow is such a complicated process that an exact solution cannot be derived in principle; one must take into account the irregular shape of particles and layered nature of snow layers with possible areas being covered by frost and sastrugi. Therefore, we believe that our approach of modeling radiative transfer in the snow–underlying surface system will be useful for the various applied problems, including the snow grain size and new fallen snow detection in polar regions, using hyperspectral SWIR measurements. The technique can also be applied to other regions and surfaces (e.g., deserts). In this case, the atmospheric correction procedure and respective expression for the similarity parameter as a function of the particle size must be modified, taking into account the spectral refractive index of light scattering particles and updates of several constants used in Equation (7).

We have found that the snow grain sizes around Aviator Glacier are about four times larger compared with those at Dome C. This leads to the increased light absorption by snow at this coastal site, which contributes to the increased rate of snow melting and formation of glacier rivers and lakes at favorable temperatures of surrounding air [33].

SNOWTRAN can be coupled with the fast infrared radiative transfer codes (see, e.g., [34]) to provide users with a tool that can be used to study various applied problems related to hyperspectral remote sensing observations in a broad spectral range from ultraviolet to the far infrared. The software is distributed upon request.

Conflicts of Interest: The authors declare no conflict of interest.

Appendix A

In this Appendix A, a simple approximate analytical equation for the snow nadir reflectance as a function of spherical albedo is proposed. In particular, we have studied the correlation between the nadir snow reflectance R_s and spherical albedo r_s for snow layers. It has been found using the radiative transfer calculations of both parameters (presented in tabular form in [15]) for the same turbid layer at g = 0.75 and the Henyey–Greenstein phase function that the following polynomial expression can be used:

$$R_s = a_0 + a_1 r_s + a_2 r_s^2, \tag{A1}$$

where the coefficients a_n can be represented by the cubic polynomial of the cosine of the solar zenith angle ξ:

$$a_n = \sum_{j=0}^{3} \Lambda_{nj} \xi_0^j. \tag{A2}$$

The parameters Λ_{nj} are given in Table A1. An important point is that the dependence of these parameters on snow microstructure can be neglected. It follows that for a nonabsorbing snow layer from Equation (A1):

$$R_{s,0} = a_0 + a_1 + a_2, \tag{A3}$$

which represents the semi-infinite nonabsorbing snow reflectance. Indeed, the variability of this parameter for the dry clean snow is low due to long paths of photons in snow in this case, which leads to the randomization of photon directions and similar values of nadir reflectance independently of the single light scattering angular characteristics of a given snow layer. We note that the TOA reflectance in the SWIR is close to the value of the snow reflectance R_s outside gaseous absorption bands in the SWIR region due to negligible atmospheric scattering effects in this region over Antarctica.

Table A1. The parameters in Equation (A2).

j/n.	0	1	2
0	0.01388	0.45760	−0.02527
1	−0.07413	1.65240	0.16899
2	0.05855	−2.78192	0.89927
3	−0.01099	1.18977	−0.41984

References

1. Stamnes, K.; Hamre, B.; Stamnes, S.; Chen, N.; Fan, Y.; Li, W.; Lin, Z.; Stamnes, J. Progress in forward-inverse modeling based on radiative transfer tools for coupled atmosphere-snow/ice-ocean systems: A review and description of the AccuRT model. *Appl. Sci.* **2018**, *8*, 2682. [CrossRef]
2. Mei, L.; Rozanov, V.; Rozanov, A.; Burrows, J.P. SCIATRAN software package (V4.6): Update and further development of aerosol, clouds, surface reflectance databases and models. *Geosci. Model Dev.* **2023**, *16*, 1511–1536. [CrossRef]

3. Nakajima, T.Y.; Murakami, H.; Hori, M.; Nakajima, T.; Aoki, T.; Oishi, T.; Tanaka, A. Efficient use of an improved radiative transfer code to simulate near-global distributions of satellite-measured radiances. *Appl. Opt.* **2003**, *42*, 3460–3471. [CrossRef] [PubMed]

4. Mayer, B.; Kylling, A. Technical note: The libRadtran software package for radiative transfer calculations—Description and examples of use. *Atmos. Chem. Phys.* **2005**, *5*, 1855–1877. [CrossRef]

5. Berk, A.; Bernstein, L.S.; Anderson, G.P.; Acharya, P.K.; Robertson, D.C.; Chetwynd, J.H.; Adler-Golden, S.M. MODTRAN cloud and multiple scattering upgrades with application to AVIRIS. *Remote Sens. Environ.* **1998**, *65*, 367–375. [CrossRef]

6. Spurr, R.; Christi, M. The LIDORT and VLIDORT linearized scalar and vector discrete ordinate radiative transfer models. In *Springer Series in Light Scattering*; Kokhanovsky, A., Ed.; Springer: Berlin/Heidelberg, Germany, 2019; pp. 1–62.

7. Ricchiazzi, P.; Yang, S.; Gautier, C.; Sowle, D. SBDART: A research and teaching software tool for plane-parallel radiative transfer in the Earth's atmosphere. *Bull. Am. Meteorol. Soc.* **1998**, *79*, 2101–2114. [CrossRef]

8. Cachorro, V.E.; Antuña-Sanchez, J.C.; de Frutos, A.M. SSolar-GOA v1.0: A simple, fast, and accurate Spectral solar radiative transfer for clear skies. *Geosci. Model Dev.* **2022**, *15*, 1689–1712. [CrossRef]

9. Cogliati, S.; Sarti, F.; Chiarantini, L.; Cosi, M.; Lorusso, R.; Lopinto, E.; Miglietta, F.; Genesio, L.; Guanter, L.; Damm, A.; et al. The PRISMA imaging spectroscopy mission: Overview and first performance analysis. *Remote Sens. Environ.* **2021**, *262*, 112499. [CrossRef]

10. Storch, T.; Honold, H.-P.; Chabrillat, S.; Habermeyer, M.; Tucker, P.; Brell, M.; Ohndorf, A.; Wirth, K.; Betz, M.; Kuchler, M.; et al. The EnMAP imaging spectroscopy mission towards operations. *Remote Sens. Environ.* **2023**, *294*, 113632. [CrossRef]

11. Rast, M.; Nieke, J.; Adams, J.; Isola, C.; Gascon, F. Copernicus Hyperspectral Imaging Mission for the Environment (Chime). In Proceedings of the 2021 IEEE International Geoscience and Remote Sensing Symposium IGARSS, Brussels, Belgium, 11–16 July 2021; pp. 108–111. [CrossRef]

12. National Academies of Sciences, Engineering, and Medicine. *Thriving on Our Changing Planet: A Decadal Strategy for Earth Observation from Space*; The National Academies Press: Washington, DC, USA, 2018. [CrossRef]

13. Sobolev, V.V. *Light Scattering in Planetary Atmospheres*; Nauka: Moscow, Russia, 1975.

14. Van de Hulst, H.C. The spherical albedo of a planet covered with a homogeneous cloud layer. *Astron. Astrophys.* **1974**, *35*, 209–214.

15. Van de Hulst, H.C. *Multiple Light Scattering, v.1, 2*; Academic Press: New York, NY, USA, 1980.

16. Kokhanovsky, A. The approximate analytical solution for the top-of-atmosphere spectral reflectance of atmosphere—Underlying snow system over Antarctica. *Remote Sens.* **2022**, *14*, 4778. [CrossRef]

17. Kokhanovsky, A.A. *Snow Optics*; Springer Nature: Cham, Switzerland, 2021.

18. Kokhanovsky, A.; Macke, A. Integral light-scattering and absorption characteristics of large nonspherical particles. *Appl. Opt.* **1997**, *36*, 8785–8790. [CrossRef]

19. Macke, A.; Müller, J.; Raschke, E. Single scattering properties of atmospheric ice crystals. *J. Atmos. Sci.* **1996**, *53*, 2813–2825. [CrossRef]

20. Shifrin, K.S. *Light Scattering in a Turbid Medium*; Gostekhteorizdat; Nauka: Leningrad, Russia, 1951.

21. Van de Hulst, H.C. *Light Scattering by Small Particles*; Wiley: New York, NY, USA, 1958.

22. Warren, S.; Brand, R.E. Optical constants of ice from the ultraviolet to the microwave: A revised compilation. *J. Geophys. Res.* **2008**, *113*, D14. [CrossRef]

23. Green, A.E.; Wagner, J.C.; Mann, A. Analytic spectral functions for atmospheric transmittance calculations. *Appl. Opt.* **1988**, *27*, 2266–2272. [CrossRef] [PubMed]

24. Guanter, L.; Kaufmann, H.; Segl, K.; Foerster, S.; Rogass, C.; Chabrillat, S.; Kuester, T.; Hollstein, A.; Rossner, G.; Chlebek, C. The EnMAP spaceborne imaging spectroscopy mission for Earth Observation. *Remote Sens.* **2015**, *7*, 8830–8857. [CrossRef]

25. Fontenla, J.N.; Harder, J.; Livingston, W.; Snow, M.; Woods, T. High-resolution solar spectral irradiance from extreme ultraviolet to far infrared. *J. Geophys. Res. Atmos.* **2011**, *116*, D20. [CrossRef]

26. Kurucz, R.L. New atlases for solar flux, irradiance, central intensity, and limb intensity. *Mem. Della Soc. Astron. Ital. Suppl.* **2005**, *8*, 189.

27. Kokhanovsky, A.A.; Brell, M.; Segl, K.; Bianchini, G.; Lanconelli, C.; Lupi, A.; Petkov, B.; Picard, G.; Arnaud, L.; Stone, R.S.; et al. First retrievals of surface and atmospheric properties using EnMAP measurements over Antarctica. *Remote Sens.* **2023**, *15*, 3042. [CrossRef]

28. Zhou, X.; Li, S.; Stamnes, K. Effects of vertical inhomogeneity on snow spectral albedo and its implication for optical remote sensing of snow. *J. Geophys. Res.* **2003**, *108*, 4738. [CrossRef]

29. Saito, M.; Yang, P.; Loeb, N.G.; Kato, S. A novel parameterization of snow albedo based on a two-layer snow model with a mixture of grain habits. *J. Atmos. Sci.* **2019**, *76*, 1419–1436. [CrossRef]

30. Gay, M.; Fily, M.; Genthon, C.; Frezzotti, M.; Oerter, H.; Winther, J.-G. Snow grain size measurements in Antarctica. *J. Glaciol.* **2002**, *48*, 527–535. [CrossRef]

31. Bianchini, G.; Belotti, C.; Di Natale, G.; Palchetti, L. Exploiting a decadal time-series of spectrally resolved downwelling infrared radiances at Dome C, Antarctica to assess the occurrence of advective warming events. In Proceedings of the EGU General Assembly 2023, Vienna, Austria, 24–28 April 2023. EGU23-1528. [CrossRef]

32. Six, D.; Fily, M.; Blarel, L.; Goloub, P. First aerosol optical thickness measurements at Dome C (East Antarctica), summer season 2003–2004. *Atmos. Environ.* **2005**, *39*, 5041–5050. [CrossRef]

33. Dombrovsky, L.A.; Kokhanovsky, A.A. Deep heating of a snowpack by solar radiation. *Front. Therm. Eng.* **2022**, *2*, 882941. [CrossRef]

34. Zhang, Z.; Yang, P.; Kattawar, G.; Huang, H.L.A.; Greenwald, T.; Li, J.; Baum, B.A.; Zhou, D.K.; Hu, Y. A fast infrared radiative transfer model based on the adding–doubling method for hyperspectral remote-sensing applications. *J. Quant. Spectrosc. Radiat. Transf.* **2007**, *105*, 243–263. [CrossRef]